Article

Integrated rocksalt–polyanion cathodes with excess lithium and stabilized cycling

Check for updates

Yimeng Huang [1], Yanhao Dong [2,3] ✉, Yang Yang [4], Tongchao Liu [5], Moonsu Yoon [3,6], Sipei Li[3], Baoming Wang [3], Ethan Yupeng Zheng [1], Jinhyuk Lee [7], Yongwen Sun [4], Ying Han[4], Jim Ciston [8], Colin Ophus [8], Chengyu Song[8], Aubrey Penn[9], Yaqi Liao[10], Haijin Ji[10], Ting Shi[10], Mengyi Liao[10], Zexiao Cheng[10], Jingwei Xiang[10], Yu Peng[11], Lu Ma[12], Xianghui Xiao [12], Wang Hay Kan [13,14], Huaican Chen[13,14], Wen Yin[13,14], Lingling Guo[15], Wei-Ren Liu[16], Rasu Muruganantham [16], Chun-Chuen Yang [17], Yuntong Zhu [1], Qingjie Li[3] & Ju Li [1,3] ✉

Co- and Ni-free disordered rocksalt cathodes utilize oxygen redox to increase the energy density of lithium-ion batteries, but it is challenging to achieve good cycle life at high voltages >4.5 V (versus Li/Li$^+$). Here we report a family of Li-excess Mn-rich cathodes that integrates rocksalt- and polyanion-type structures. Following design rules for cation filling and ordering, we demonstrate the bulk incorporation of polyanion groups into the rocksalt lattice. This integration bridges the two primary families of lithium-ion battery cathodes—layered/spinel and phosphate oxides— dramatically enhancing the cycling stability of disordered rocksalt cathodes with 4.8 V upper cut-off voltage. The cathode exhibits high gravimetric energy densities above 1,100 Wh kg^{-1} and >70% retention over 100 cycles. This study opens up a broad compositional space for developing battery cathodes using earth-abundant elements such as Mn and Fe.

Rapid growth of electricity storage capabilities with lithium-ion batteries (LIBs) is required to realize a sustainable energy infrastructure[1]. In terms of resources, Co is ~5× the price of Li on a molar basis[2,3], and Ni is ~2× (ref. 3); thus, we would run into Co or Ni crises before Li. For advanced LIB cathodes, eliminating Co and Ni usage would greatly improve the scalability of electricity storage[4]. Disordered rocksalt (DRX) cathodes[5,6] are attractive for being potentially Co- and Ni-free, while having high energy densities (approaching 1,100 Wh kg^{-1} (ref. 7)). On the other hand, to reach high energy densities (>900 Wh kg^{-1}), high upper cut-off voltages (for example, 4.8 V versus Li/Li$^+$ for DRX[7–11]) are required for cathodes, which means highly delithiated states with most of the Li$^+$-hosting sites vacant. This often triggers the participation of oxygen anion redox and eventually irreversible oxygen loss, as delithiation lowers the Fermi level towards or dropping below the top of the oxygen 2p band, especially at the surface and interfaces[6,12–14]. A heavy usage of hybrid anion- and cation-redox with more exotic oxygen valence O$^{\alpha-}$ (0 < α < 2) challenges the cycling stability of the cathode since O$^{\alpha-}$ tends to be more mobile, leading to percolating lattice oxygen diffusion to the reactive surface, extensive side reactions with the electrolyte and finally structural and chemical instability at the surface and in the bulk[15–19]. These are critical issues for DRX[6,20] and other high-energy-density cathodes[16,21].

LIB cathodes are mainly constructed on face-centred cubic (FCC) oxygen or lower-symmetry polyanion framework (hexagonal close-packed, HCP, oxygen for LiFePO$_4$, the most useful polyanion cathode). The former has cation ordering in the parent rocksalt structure, which includes high-energy-density cathodes of LiCoO$_2$, Ni-rich layered cathodes and Li-/Mn-rich layered cathodes[22,23] (spinel and DRX cathodes are also rocksalt structure derivatives with FCC oxygen sublattice). They have high theoretical capacities >270 mAh g^{-1}, and extensive research has been conducted to improve their high-voltage stability. The latter is exemplified by LiFePO$_4$, with exceptional structural, electrochemical and thermal stability, yet limited by the low theoretical capacity (170 mAh g^{-1}) and low energy density at the cathode level[24–26].
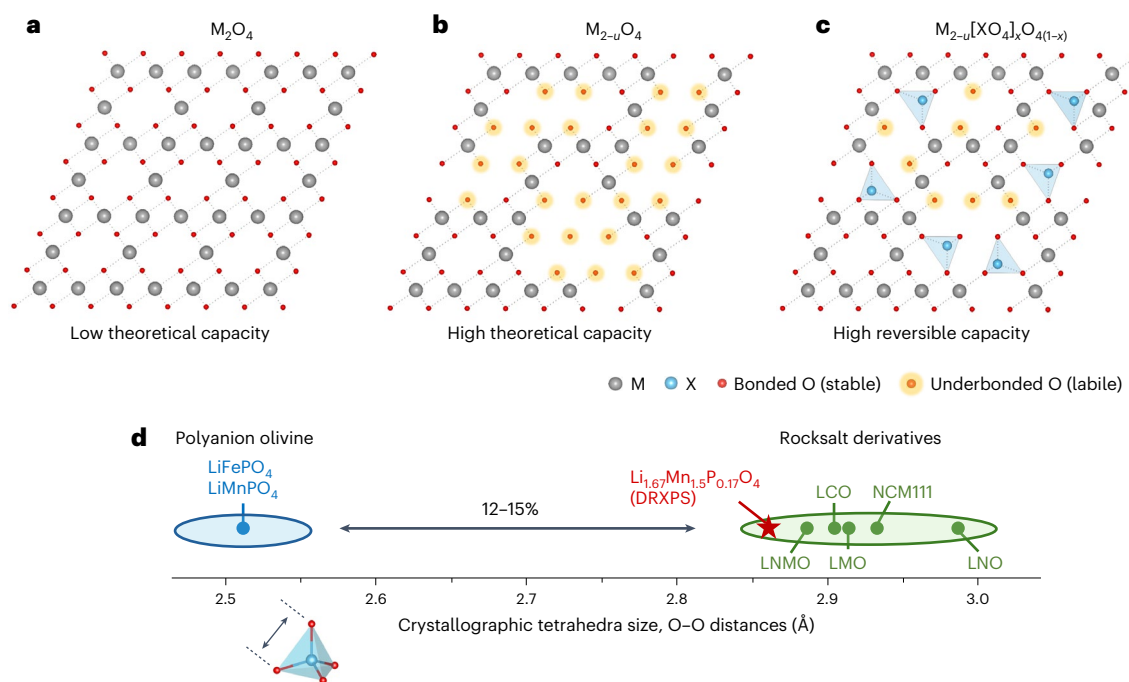
Fig. 1 | Design of DRXPS cathodes. a, The structure of M_2O_4. **b**, The structure of $M_{2-u}O_4$. **c**, The structure of $M_{2-u}[XO_4]_xO_{4(1-x)}$. **d**, Comparison of crystallographic tetrahedra size for polyanion olivine and rocksalt-type cathodes. LMO, $LiMn_2O_4$; LNMO, $LiNi_{0.5}Mn_{1.5}O_4$; LCO, $LiCoO_2$; NCM111, $LiNi_{1/3}Co_{1/3}Mn_{1/3}O_2$; LNO, $LiNiO_2$.

Marriage between the two families may offer synergistically improved energy density and stability. However, few reports[27] of their integration testify to the incompatibility between rocksalt and polyanion structures.

This work seeks to resolve the above conundrum with the invention of integrated rocksalt–polyanion cathodes. These compositions originate from DRX chemistries, and a major effort here is to improve the cycling stability under high upper cut-off voltages (required to deliver high capacity and energy density). We successfully produced a family of Li-excess Co- and Ni-free disordered rocksalt–polyanionic spinel (DRXPS) cathodes, with a general chemical formula of $Li_{2+u-v}M_{2-u}[XO_4]_xO_{4(1-x)}$. Here, M denotes transition metals such as Mn and Fe, XO_4 denotes polyanion groups such as PO_4, SiO_4 and SO_4, and u, v and x describe the designed stoichiometries. This family of compounds is called DRXPS because they are designed on a parent DRX structure and have bulk polyanion incorporation and spinel-type cation ordering (that gives a spinel diffraction pattern). Remarkable improvements of the cycling stability over reported DRX cathodes have been achieved in $Li_{1.67}Mn_{1.5}P_{0.17}O_4$, $Li_{1.67}Mn_{1.5}B_{0.17}O_4$, $Li_{1.67}Mn_{1.25}Fe_{0.25}P_{0.17}O_4$ and four more compositions, all belonging to the DRXPS family. The DRXPS cathodes have high capacities (>350 mAh g^{-1}), high energy densities (>1,100 Wh kg^{-1}), stable cycling (>70% energy density retention over 100 cycles), good rate performance and a highly tunable compositional space. The general design principles and experimental efforts presented here offer avenues for the future development of Co- and Ni-free cathodes.

Materials design

Our task is to design high-capacity oxide cathodes with excess Li, anion redox activity, bulk polyanion incorporation and good electrochemical stability. Starting from the high-capacity FCC oxygen framework, a three-dimensionally connected spinel structure M_2O_4 (Fig. 1a, Li is not shown for simplicity) provides the best hybridization between transition metal (M) d and oxygen $2p$ orbitals under the constrained Li/M molar ratio of 1 (each oxygen is coordinated with one tetrahedral Li and three octahedral M). Further raising the Li/M molar ratio above 1 (that is, replacing some M in Fig. 1a by Li) increases the theoretical capacity, and anion redox is simultaneously activated with underbonded

oxygen (Fig. 1b). These underbonded oxygen can be oxidized upon charging to high voltages and may eventually leave the lattice in the form of outgassing if a percolative kinetic pathway exists from the bulk to the surface[28]. We aim to shut down the labile oxygen percolation by incorporating some polyanion groups into the Li-excess lattice (Fig. 1c), utilizing the strong X–O covalent bonds to mitigate oxygen instability.

Practical realization of the above is challenging and comes to the same incompatibility issue between rocksalt and polyanion structures discussed above. The main reasons are twofold. First, the cations in polyanion cathodes are not close-packed. The octahedral sites face-shared with XO_4 tetrahedra need to be empty[24]. This conflicts with cation-filling rules in layered and DRX cathodes (the octahedral sites are fully occupied). Second, X–O covalent bonds are short and strong, which results in much shorter O–O distances (characterizing the tetrahedral size) than the ones in rocksalt-structure cathodes. For example, the true tetrahedra size calculated from the P–O bond length in the polyanion olivine cathode $LiFePO_4$ (refs. 29,30) is 12–15% smaller than that in rocksalt-structure cathodes[31–34] (Fig. 1d). This would result in large lattice distortion and, thus, difficulty in making a solid-solution phase between XO_4 polyanions and 'normal O' anions.

We propose the following solution to the two problems mentioned above. For the first one, cation deficiency is an effective approach. Specifically, we were inspired by the polyhedral occupation rules in spinel cathodes: octahedra at 16d sites are fully occupied, and octahedra at 16c sites (face-shared with tetrahedra at 8a sites) are empty. So spinel-like cation ordering is preferred. For the second one, typical high-temperature solid-state synthesis would not work, and we resort to lower-temperature mechanochemical synthesis. Without going into the detailed derivations of the optimal values of stoichiometry (u, v and x) in Supplementary Note 1, we show in the following sections that the above simple design rules are powerful enough to guide the synthesis of the DRXPS cathode series.

Structure and morphology of prototype $Li_{1.67}Mn_{1.5}P_{0.17}O_4$

A prototype DRXPS cathode $Li_{1.67}Mn_{1.5}P_{0.17}O_4$ was synthesized by a one-pot mechanochemical method. The obtained sample has a
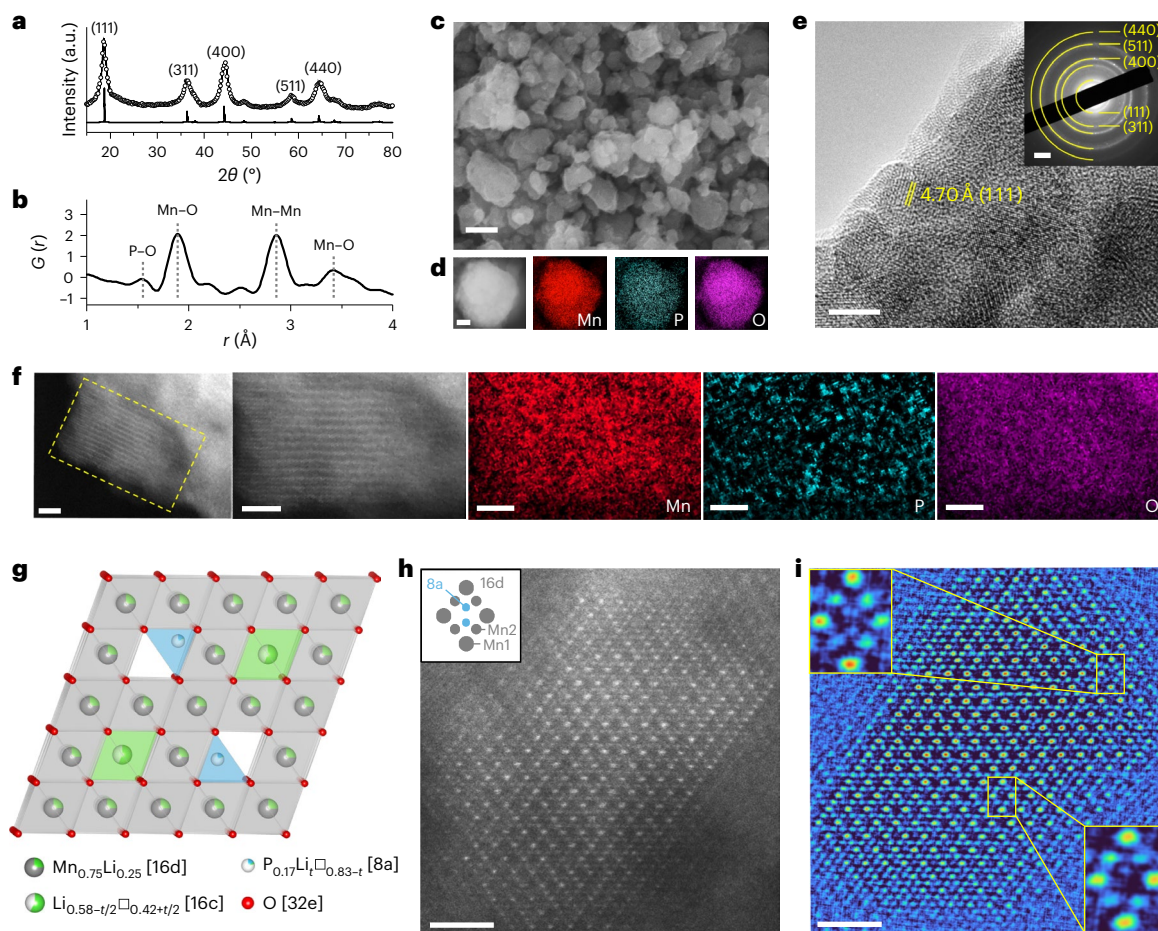
Fig. 2 | Structural characterization of $Li_{1.67}Mn_{1.5}P_{0.17}O_4$. a, XRD patterns of $Li_{1.67}Mn_{1.5}P_{0.17}O_4$. Open black circles are experimental, and solid black line is calculated. **b**, PDF of $Li_{1.67}Mn_{1.5}P_{0.17}O_4$. $G(r) = 4\pi r(\rho(r) - \rho_0)$, where $\rho(r)$ is the local atomic number density at distance r from a reference atom, and ρ_0 is the average atomic density of the material. **c**, SEM image of $Li_{1.67}Mn_{1.5}P_{0.17}O_4$. Scale bar, 200 nm. **d**, STEM–EDS mapping of $Li_{1.67}Mn_{1.5}P_{0.17}O_4$. Scale bar, 100 nm. **e**, TEM image of $Li_{1.67}Mn_{1.5}P_{0.17}O_4$. Scale bar, 5 nm. Inset: SAED pattern. Scale bar, 2 nm^{-1}. **f**, STEM–EELS mapping of Mn, P and O, performed on a single-crystal grain close

to a zone axis, as indicated by the yellow dashed box. Note that the EELS signal of P is very weak due to the small atomic ratio of P in the composition; thus, the data supports but does not prove the uniform spatial distribution of P. Scale bars, 2 nm. **g**, Structural model of $Li_{1.67}Mn_{1.5}P_{0.17}O_4$. **h**, HAADF-STEM image of $Li_{1.67}Mn_{1.5}P_{0.17}O_4$. Inset: Atomic positions with alternating intensities at 16d sites, characteristic of a spinel structure. Scale bar, 1 nm. **i**, Filtered image of **h**. Insets: 16d and 8a site signals. Scale bar, 1 nm.

composition close to the designed stoichiometry (shown by the inductively coupled plasma mass spectrometry (ICP-MS) data in Supplementary Table 1). Its X-ray diffraction (XRD) pattern (Fig. 2a) matches with a single-phase cubic spinel structure ($a = b = c$, $\alpha = \beta = \gamma = 90°$; Supplementary Fig. 1). Rietveld refinement yields a lattice constant $a = 8.1527$ Å (Supplementary Fig. 1 and Supplementary Table 2), which is slightly smaller than those of spinel cathodes (8.246 Å for $LiMn_2O_4$ and 8.172 Å for $LiNi_{0.5}Mn_{1.5}O_4$). Neutron powder diffraction measurement (Supplementary Fig. 2) and refinement (Supplementary Table 3) were further conducted on $Li_{1.67}Mn_{1.5}P_{0.17}O_4$ for better sensitivity on Li sites, which shows consistent results with XRD measurements. For more structural information, we conducted pair distribution function (PDF) analysis on $Li_{1.67}Mn_{1.5}P_{0.17}O_4$ (Fig. 2b) and compared with references of $LiMn_2O_4$ and $LiFePO_4$ (Supplementary Fig. 3). First-nearest-neighbour P–O pair at 1.549 Å was observed, which is slightly longer than the P–O pair in the PO_4 group of $LiFePO_4$ (1.520 Å). First-nearest-neighbour Mn–O pair at 1.893 Å and Mn–Mn pair 2.858 Å were observed, which are slightly shorter than the corresponding ones in $LiMn_2O_4$ (1.903 Å for Mn–O and 2.887 Å for Mn–Mn). These elastic straining effects are consistent with our materials design (tensile strained for XO_4 compared with $LiFePO_4$ and compressive strained for MO_6 compared with $LiMn_2O_4$). The effect smears at longer distances, for example, second-nearest-neighbour

Mn–O distances (3.418 Å) are similar in $Li_{1.67}Mn_{1.5}P_{0.17}O_4$ and $LiMn_2O_4$. Raman spectroscopy measurement (Supplementary Fig. 4) was conducted for local structure analysis. The Raman peak at ~940 cm^{-1} can be assigned to the A_{1g} mode of PO_4 (ref. 35), the peak at ~600 cm^{-1} can be assigned to the symmetric stretching mode of MnO_6 (refs. 36,37) and the peaks at 420–490 cm^{-1} can be assigned to the symmetric stretching modes of LiO_4 and LiO_6 (ref. 36). These Raman features support tetrahedral occupation of P, octahedral occupation of Mn and mixed tetrahedral/octahedral occupations of Li.

The scanning electron microscopy (SEM) image in Fig. 2c shows that $Li_{1.67}Mn_{1.5}P_{0.17}O_4$ has an average size of ~150 nm for the agglomerates (see size distribution in Supplementary Fig. 5). Energy dispersive spectroscopy mapping in scanning transmission electron microscopy (STEM-EDS) (Fig. 2d) shows a uniform distribution of Mn, P and O. The transmission electron microscopy (TEM) image in Fig. 2e shows that the particles in Fig. 2c are polycrystalline, consisting of 5–10 nm 'primary' particles that are crystalline. A characteristic lattice spacing $d = 4.70$ Å can be identified, corresponding to the (111) plane of the spinel structure. The selected area electron diffraction (SAED) pattern (Fig. 2e, inset) further confirms the polycrystallinity, with diffraction rings corresponding to the (111), (311), (400), (511) and (440) peaks. Figure 2f shows the electron energy loss spectroscopy (EELS) mapping
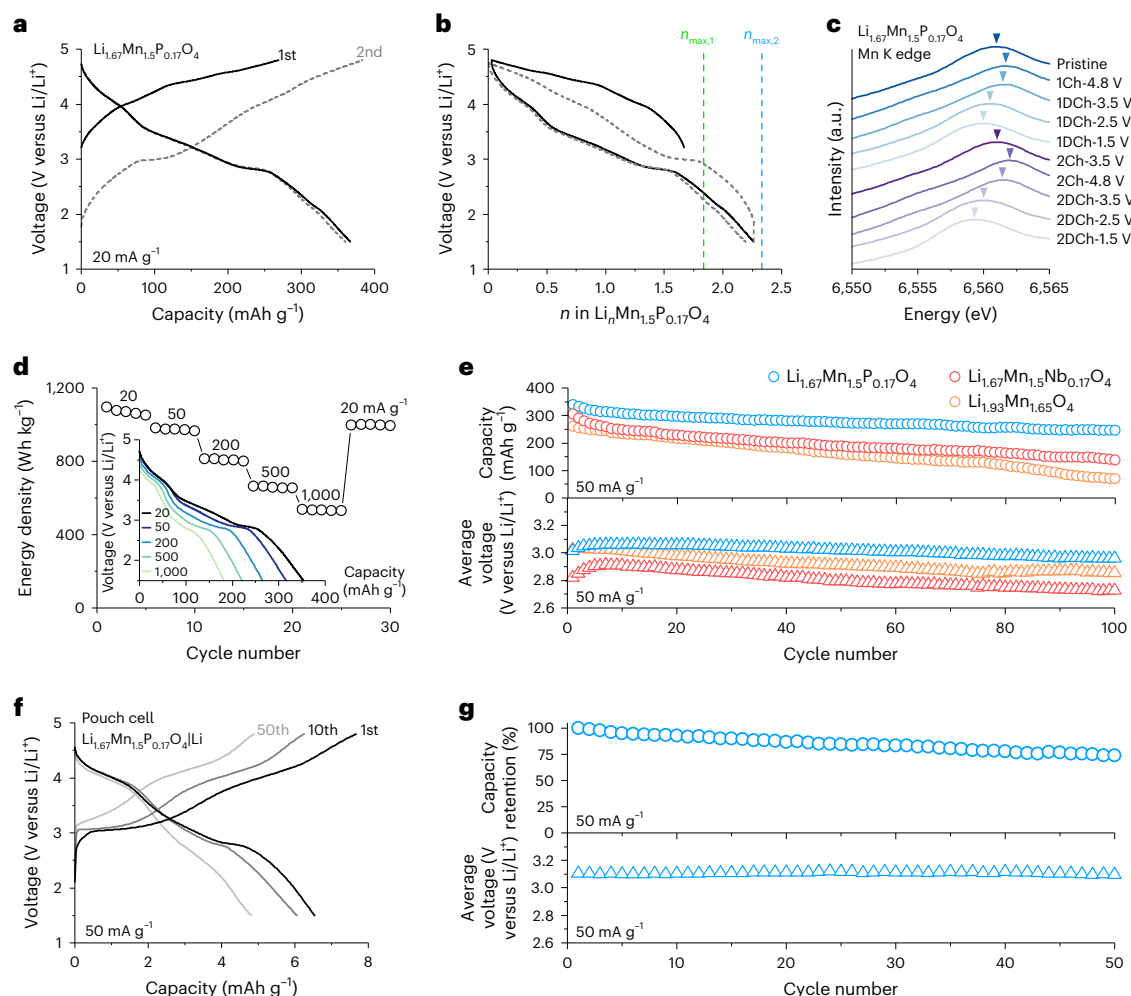
Fig. 3 | Electrochemistry and redox mechanism of $Li_{1.67}Mn_{1.5}P_{0.17}O_4$. a, Voltage profiles of $Li_{1.67}Mn_{1.5}P_{0.17}O_4$ in the initial two formation cycles between 1.5 and 4.8 V versus Li/Li$^+$ at 20 mA g^{-1}. **b**, Capacity from **a** converted to Li content n. The theoretical capacity is marked by the dashed lines under two assumptions: if Li tetrahedral occupation is not allowed (dashed green line); if Li tetrahedral occupation is allowed (dashed blue line). **c**, Mn K-edge XANES spectra of $Li_{1.67}Mn_{1.5}P_{0.17}O_4$ in the first two cycles. **d**, Rate performance test of $Li_{1.67}Mn_{1.5}P_{0.17}O_4$ at 20, 50, 200, 500 and 1,000 mA g^{-1} (the same cell was used). Inset: Voltage profiles of the first discharge cycle at 20, 50, 200, 500 and 1,000 mA g^{-1}.
e, Discharge capacity (top) and average discharge voltage (bottom) retention of $Li_{1.67}Mn_{1.5}P_{0.17}O_4$, $Li_{1.67}Mn_{1.5}Nb_{0.17}O_4$ and $Li_{1.93}Mn_{1.65}O_4$ in 100 cycles between 1.5 and 4.8 V versus Li/Li$^+$ at 50 mA g^{-1}, following the two initial formation cycles at 20 mA g^{-1} (not shown). **f**, Voltage profiles of ($Li_{1.67}Mn_{1.5}P_{0.17}O_4$|Li) pouch cell at the 1st, 10th and 50th cycle between 1.5 and 4.8 V versus Li/Li$^+$ at 50 mA g^{-1} (following two formation cycles at 20 mA g^{-1}). **g**, Discharge capacity (top) and average discharge voltage (bottom) retention of the pouch cell during 50 mA g^{-1} cycling.

of a $Li_{1.67}Mn_{1.5}P_{0.17}O_4$ primary particle, with uniform Mn, P and O distributions that support the bulk incorporation of P in the lattice (additional evidence from STEM-EDS is shown in Supplementary Fig. 6).

With the above information, we constructed the structural model (Fig. 2g). Per chemical formula $Li_{1.67}Mn_{1.5}P_{0.17}O_4$, 4 O at 32e sites form the FCC anion framework, 1.5 Mn occupy 3/4 of the 16d cation octahedral sites and 0.17 P occupy 1/6 of the 8a cation tetrahedral sites. As 16d sites should be fully occupied in spinel structure, the remaining 1/4 should be occupied by 0.5 Li. This leaves 1.17 Li that occupy either 8a or 16c sites. Therefore, using '□' to denote cation vacancy (that is, unoccupied tetrahedral/octahedral sites), we can express the structural model as $(P_{0.17}Li_t□_{0.83-t})_{8a}(Li_{1.17-t}□_{0.83+t})_{16c}(Li_{0.5}Mn_{1.5})_{16d}(O_4)_{32e}$. The calculated XRD pattern from the constructed structure (Fig. 2a, solid black curve) matches well with the experimental one, and it is close to the refined structure (Supplementary Table 2). The proposed structural model is further supported by high-angle annular dark-field scanning transmission electron microscopy (HAADF-STEM) image in Fig. 2h. Spinel-type cation ordering with Mn atoms at 16d octahedral sites, viewed along the [110] zone axis, is clearly shown. The alternating intensities at 16d sites (brighter at Mn1 sites and darker at Mn2 sites; schematics shown

in the inset of Fig. 2h) are also a characteristic feature of the spinel structure[38,39]. Further analysis using a least absolute shrinkage and selection operator (LASSO) filter (Methods) was applied to obtain Fig. 2i. In addition to 16d site signals, some intensities are present at 8a sites (see top-left and bottom-right insets of Fig. 2i). These 8a site signals are possibly attributed to P, as Li has almost no contrast under the HAADF mode and it is difficult for Mn to enter tetrahedral sites.

Electrochemistry and redox mechanism of $Li_{1.67}Mn_{1.5}P_{0.17}O_4$

We first evaluated the electrochemical performance of $Li_{1.67}Mn_{1.5}P_{0.17}O_4$ in coin-type half cells between 1.5 and 4.8 V versus Li/Li$^+$ at room temperature. Figure 3a shows the galvanostatic charge–discharge curves of the first two cycles at 20 mA g^{-1}, with high discharge capacities of ~365 mAh g^{-1} and high discharge energy densities of ~1,120 Wh kg^{-1}. Converting the capacity to stoichiometry, we estimated a high Li usage of 1.63 Li removal (out of 1.67 Li) per formula unit (Fig. 3b) in the first charge. Since Mn in $Li_{1.67}Mn_{1.5}P_{0.17}O_4$ has an average valence of +3.67 (a slightly lower Mn average valence may be possible depending on synthesis conditions) and Mn^{3+}/Mn^{4+} can only charge-compensate
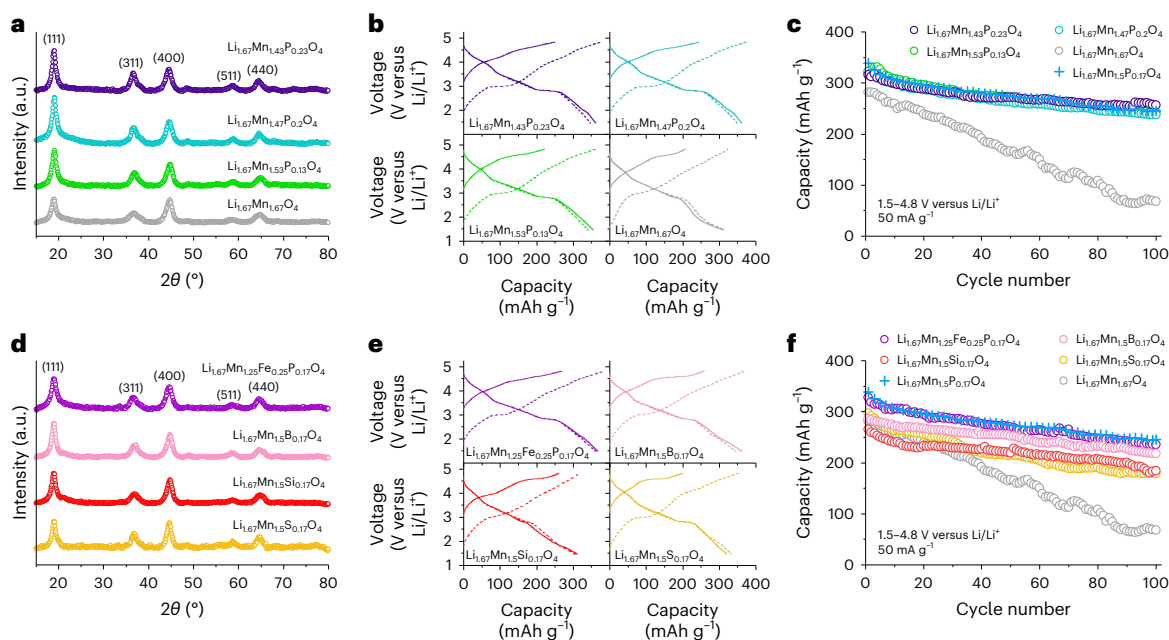
Fig. 4 | Structure and performance of diverse compositions of DRXPS.
a, XRD patterns of $Li_{1.67}Mn_{1.67-x}P_xO_4$ ($x = 0, 0.13, 0.2, 0.23$). **b**, Voltage profiles of the initial two formation cycles of $Li_{1.67}Mn_{1.67-x}P_xO_4$ ($x = 0, 0.13, 0.2$ and 0.23) between 1.5 and 4.8 V versus Li/Li^+ at 20 mA g^{-1}. **c**, Discharge capacity retention of $Li_{1.67}Mn_{1.67-x}P_xO_4$ ($x = 0, 0.13, 0.17, 0.2$ and 0.23) in the first 100 cycles, between 1.5 and 4.8 V versus Li/Li^+ at 50 mA g^{-1}, after two formation cycles at 20 mA g^{-1} (not shown). **d**, XRD patterns of $Li_{1.67}Mn_{1.25}Fe_{0.25}P_{0.17}O_4$ and $Li_{1.67}Mn_{1.5}X_{0.17}O_4$ (X = B, Si, S).

e, Voltage profiles of the initial two formation cycles of $Li_{1.67}Mn_{1.25}Fe_{0.25}P_{0.17}O_4$ and $Li_{1.67}Mn_{1.5}X_{0.17}O_4$ (X = B, Si, S) between 1.5 and 4.8 V versus Li/Li^+ at 20 mA g^{-1}.
f, Discharge capacity retention of $Li_{1.67}Mn_{1.25}Fe_{0.25}P_{0.17}O_4$ and $Li_{1.67}Mn_{1.5}X_{0.17}O_4$ (X = B, Si, S) in the first 100 cycles, between 1.5 and 4.8 V versus Li/Li^+ at 50 mA g^{-1}, after two formation cycles at 20 mA g^{-1} (not shown). Data for $Li_{1.67}Mn_{1.5}P_{0.17}O_4$ and $Li_{1.67}Mn_{1.67}O_4$ are also shown for reference.

for 0.5 Li removal, we expect active participation of anion redox $O^{2-}/O^{\alpha-}$ ($0 < \alpha < 2$). During the first discharge, 2.23 Li was inserted into the structure, ending with an over-lithiated composition of $Li_{2.27}Mn_{1.5}P_{0.17}O_4$. The over-lithiation should be charge-compensated by Mn reduction. The second cycle shows a similar discharge curve to the first one, indicating good reversibility.

To better understand the redox mechanism, we performed ex situ hard X-ray absorption spectroscopy. Figure 3c shows the Mn K-edge X-ray absorption near-edge structure (XANES) for $Li_{1.67}Mn_{1.5}P_{0.17}O_4$ at different states of charge (marked on the voltage profiles in Supplementary Fig. 7b). Since the near-edge structure depends on both the oxidation state and the bonding environment[40], we analysed Mn valence by comparing with reference spectra (Supplementary Fig. 7a). For the first two cycles, all Mn K-edge spectra stay higher in energy than the Mn_2O_3 (Mn^{3+}) reference and shift to higher energy (Mn oxidation) during charge and to lower energy (Mn reduction) during discharge, indicating active participation of reversible $Mn^{3+/4+}$ redox couple. For charge in the first (pristine to 1Ch-4.8V) and second cycle (1DCh-1.5V to 2Ch-4.8V), capacities of 269 and 384 mAh g^{-1} are observed (corresponding to Mn valence changes of +1.09 and +1.56), respectively. Meanwhile, Mn K edges for both charge half-cycles shift from between the Mn_2O_3 (Mn^{3+}) and MnO_2 (Mn^{4+}) reference spectra to close to MnO_2 (Mn^{4+}). This one-electron TM redox cannot account for the high reversible capacity by itself. For discharge to 3.5 V versus Li/Li^+ (1Ch-4.8V to 1DCh-3.5V and 2Ch-4.8V to 2DCh-3.5V), a capacity of ~96 mAh g^{-1} (corresponding to a Mn valence change of −0.39) are observed for both cycles, while the Mn K edges for both only experience minor downshifts. Therefore, active oxygen redox should also be involved during charge to 4.8 V versus Li/Li^+ and discharge to 3.5 V versus Li/Li^+ for the initial two cycles. Capacities below 3.5 V versus Li/Li^+ should be solely contributed by the $Mn^{3+/4+}$ redox couple since the Mn K edges lie between the Mn_2O_3 (Mn^{3+}) and MnO_2 (Mn^{4+}) spectra, and the shifts roughly match the expected Mn valence change (converted from the observed capacity). Towards the end of discharge, the average Mn valence stayed above +3, as shown by

the extra ex situ measurements on the Mn K edge performed in the low voltage region (<2.5 V versus Li/Li^+) (Supplementary Fig. 8). This means that the population of Mn^{2+}, prone to dissolution in the electrolyte, is low in the cathode.

The rate performance of $Li_{1.67}Mn_{1.5}P_{0.17}O_4$ was tested from 20 mA g^{-1} to 1,000 mA g^{-1} (~5.5 C calculated from the charging time). Capacity retentions of 75% and 51% were observed when the galvanostatic current density increased from 20 mA g^{-1} to 200 mA g^{-1} and 1,000 mA g^{-1}, respectively (Fig. 3d and Supplementary Fig. 9). Galvanostatic intermittent titration technique (GITT) measurement was performed in the first discharge cycle for $Li_{1.67}Mn_{1.5}P_{0.17}O_4$ and polyanion-free reference sample $Li_{1.93}Mn_{1.65}O_4$ (Supplementary Fig. 10a). The former shows an average non-Ohmic loss of only 90 mV per titration step (Supplementary Fig. 10b). The calculated Li diffusivities are in the range of ~10^{-14} to 10^{-13} cm^2 s^{-1} (Supplementary Fig. 10c), which are higher than the commonly reported values (10^{-16} to 10^{-15} cm^2 s^{-1}) for DRX cathodes[20]. This shows facile Li^+ diffusion kinetics for the cation-deficient spinel structure of DRXPS. Comparing the non-Ohmic losses with $Li_{1.93}Mn_{1.65}O_4$ (Supplementary Fig. 10b), we found that the addition of polyanions in DRXPS does not harm Li^+ diffusion kinetics. The cycling performance of $Li_{1.67}Mn_{1.5}P_{0.17}O_4$ was tested at 50 mA g^{-1} between 1.5 and 4.8 V versus Li/Li^+, after two formation cycles at 20 mA g^{-1}. After 100 cycles, it has a capacity retention of 72% (Fig. 3e, top), an average discharge voltage maintained at >3 V versus Li/Li^+ (minimal voltage decay of <0.74 mV per cycle; Fig. 3e, bottom) and a discharge energy retention of 71% (Supplementary Fig. 11). For comparison, we tested the cycling performance of the similarly synthesized polyanion-free $Li_{1.67}Mn_{1.5}Nb_{0.17}O_4$ and $Li_{1.93}Mn_{1.65}O_4$ as control groups (Supplementary Fig. 12; both have spinel-like structures, and an average Mn valence of +3.67, similar to $Li_{1.67}Mn_{1.5}P_{0.17}O_4$). $Li_{1.67}Mn_{1.5}Nb_{0.17}O_4$/$Li_{1.93}Mn_{1.65}O_4$ show faster degradations with 45%/27% capacity retention (Fig. 3e, top) and 44%/25% energy density retention (Supplementary Fig. 11) after 100 cycles under the same testing conditions. dQ/dV analysis for $Li_{1.67}Mn_{1.5}P_{0.17}O_4$ and $Li_{1.93}Mn_{1.65}O_4$ (Supplementary Fig. 13) provides better visualization

of the improved oxygen redox reversibility at high voltages (>4.2 V versus Li/Li$^+$) for $Li_{1.67}Mn_{1.5}P_{0.17}O_4$. Remarkably, $Li_{1.67}Mn_{1.5}P_{0.17}O_4$ have suppressed gas evolution (in situ differential electrochemical mass spectrometry, DEMS, in Supplementary Fig. 14), Mn dissolution in the electrolyte (Supplementary Fig. 15a) and Mn deposition on the anode (Supplementary Fig. 15b) compared with $Li_{1.67}Mn_{1.5}Nb_{0.17}O_4$, all indicating stability enhancement in the former composition (more detailed comparisons between $Li_{1.67}Mn_{1.5}P_{0.17}O_4$ and $Li_{1.67}Mn_{1.5}Nb_{0.17}O_4$ are provided in Supplementary Note 2). The high-voltage cycling stability of $Li_{1.67}Mn_{1.5}P_{0.17}O_4$ is also superior over the DRX cathodes reported in the literature (see comparison in Supplementary Table 4 and Supplementary Fig. 16). Lastly, to evaluate the electrochemical performance of $Li_{1.67}Mn_{1.5}P_{0.17}O_4$ under more practically relevant conditions, we assembled $Li_{1.67}Mn_{1.5}P_{0.17}O_4$|Li metal anode pouch cells. A good capacity retention of 74% and stable discharge voltage around 3.11 V (Fig. 3f,g, with no voltage decay) have been achieved over 50 cycles at 50 mA g^{-1} between 1.5 and 4.8 V versus Li/Li$^+$. In addition, we fabricated thicker electrodes with higher active material weight ratio and achieved good cycling stability when the active material mass loading is increased to 5–10 mg cm^{-2} (Supplementary Fig. 17).

Exploring compositional space of DRXPS

The DRXPS family has a rich chemistry. To demonstrate, we show the following examples within the general formula $Li_{2+u-v}M_{2-u}[XO_4]_xO_{4(1-x)}$. We first varied the P content in $Li_{1.67}Mn_{1.67-x}P_xO_4$ ($0 \le x \le 0.5$). The XRD patterns of the four synthesized compounds are shown in Fig. 4a (more examples in Supplementary Fig. 18a). Phase-pure spinel structure readily forms at $x \le 0.27$, while the impurity phase begins to form at $x \ge 0.33$ (from unreacted MnO_2 precursor). To evaluate the electrochemical performance, we cycled $Li_{1.67}Mn_{1.67-x}P_xO_4$ at 50 mA g^{-1} between 1.5 and 4.8 V versus Li/Li$^+$, after two formation cycles at 20 mA g^{-1}. Figure 4b shows the voltage profiles of the four selected compositions in the initial two formation cycles. As shown in Fig. 4c and Supplementary Fig. 18b, PO_4 incorporation drastically improves the cycling stability over the P-free $Li_{1.67}Mn_{1.67}O_4$. For better quantifications, we compared the discharge energy density at the 25th cycle at 50 mA g^{-1} (Supplementary Fig. 18c) and benchmarked against 730 Wh kg^{-1} reported by Ji et al.[7] for DRX and related cathodes. We found that the relation between x and cycling performance resembles that of a volcano plot (also true at the 100th cycle; Supplementary Fig. 18d), and $0.13 \le x \le 0.23$ offers stabilized energy density of 867–890 Wh kg^{-1} at the 25th cycle. The experimentally observed volcano plot behaviour and x range are quantitatively consistent with analytical derivations ($0.159 \le x \le 0.222$ in Supplementary Note 1) based on our stated design principles. A detailed study of the compositions with varying u and v is provided in Supplementary Note 3.

We next practiced Mn–Fe substitution. Fe is another redox-active and earth-abundant element that attracts continuous interest. $Li_{1.67}Mn_{1.25}Fe_{0.25}P_{0.17}O_4$ was synthesized mechanochemically. The XRD pattern shows a single-phase cubic spinel structure (Fig. 4d; $a = b = c = 8.129$ Å, $\alpha = \beta = \gamma = 90°$). Under SEM, we confirmed that $Li_{1.67}Mn_{1.25}Fe_{0.25}P_{0.17}O_4$ consisted of polycrystalline particles (~200 nm; Supplementary Fig. 19a) with uniform elemental distributions (EDS mapping in Supplementary Fig. 19b) and fine primary nano particles (TEM in Supplementary Fig. 19c; a characteristic lattice spacing of 4.69 Å, corresponding to the (111) peak of the spinel structure, and SAED in the inset of Supplementary Fig. 19c showing polycrystalline diffraction rings that also match the phase). The electrochemical performance of $Li_{1.67}Mn_{1.25}Fe_{0.25}P_{0.17}O_4$ was tested between 1.5 and 4.8 V versus Li/Li$^+$ at room temperature. In the first cycle at 20 mA g^{-1} (Fig. 4e), it shows a discharge capacity of 327 mAh g^{-1} and a discharge energy density of 978 Wh kg^{-1}, which are slightly lower than the corresponding values for $Li_{1.67}Mn_{1.5}P_{0.17}O_4$. $Li_{1.67}Mn_{1.25}Fe_{0.25}P_{0.17}O_4$ shows exceptional cycling performance, with 72% capacity retention (Fig. 4f) and 67% energy density retention (Supplementary Fig. 20b) over 100 cycles at 50 mA g^{-1}. The substitution was extended to a higher Fe ratio to produce

$Li_{1.67}MnFe_{0.5}P_{0.17}O_4$ and with some Ni to produce $Li_{1.67}Mn_{1.33}Ni_{0.17}P_{0.17}O_4$. The spinel phase has been identified for all these compositions (Supplementary Fig. 20a). Their cycling performances are compared with $Li_{1.67}Mn_{1.5}P_{0.17}O_4$ and $Li_{1.67}Mn_{1.25}Fe_{0.25}P_{0.17}O_4$ in Supplementary Fig. 20b. Discharge energy densities of 610–825 Wh kg^{-1} were obtained at the 25th cycle (Supplementary Fig. 20c), which demonstrates highly tunable transition metal chemistries in DRXPS.

We lastly studied different polyanion groups. In addition to the valence +5 P, we synthesized $Li_{1.67}Mn_{1.5}X_{0.17}O_4$ with X = +3 B, +4 Si and +6 S. These non-metallic elements all form strong covalent bonds with oxygen and can adopt a tetrahedral occupancy (that is, forming XO_4 groups). As shown by the XRD patterns in Fig. 4d, phase-pure spinel structures have been identified for $Li_{1.67}Mn_{1.5}B_{0.17}O_4$ and $Li_{1.67}Mn_{1.5}Si_{0.17}O_4$, while minor impurity peaks matching MnO_2 (precursor) exists in $Li_{1.67}Mn_{1.5}S_{0.17}O_4$ in addition to the main spinel phase. Microscopy characterizations in Supplementary Fig. 19d–f of a selected composition, $Li_{1.67}Mn_{1.5}B_{0.17}O_4$, show a polycrystalline particle morphology with ultrafine primary ones that are well crystalized. The electrochemical performance of $Li_{1.67}Mn_{1.5}X_{0.17}O_4$ was tested between 1.5 and 4.8 V versus Li/Li$^+$ at room temperature. Figure 4e shows the galvanostatic charge–discharge curves of the first two cycles at 20 mA g^{-1} for $Li_{1.67}Mn_{1.5}B_{0.17}O_4$, $Li_{1.67}Mn_{1.5}Si_{0.17}O_4$ and $Li_{1.67}Mn_{1.5}S_{0.17}O_4$. Among the three compositions, $Li_{1.67}Mn_{1.5}B_{0.17}O_4$ has the highest discharge capacity of ~360 mAh g^{-1} and the highest discharge energy density of ~1,070 Wh kg^{-1}, which are comparable with the corresponding values of $Li_{1.67}Mn_{1.5}P_{0.17}O_4$. When cycled at a higher rate of 50 mA g^{-1}, good cycling stability can be identified and the discharge capacity (Fig. 4f) and energy density (Supplementary Fig. 21) at the 25th cycle (after two formation cycles) follows the rank of $Li_{1.67}Mn_{1.5}P_{0.17}O_4$ > $Li_{1.67}Mn_{1.5}B_{0.17}O_4$ > $Li_{1.67}Mn_{1.5}S_{0.17}O_4$ > $Li_{1.67}Mn_{1.5}Si_{0.17}O_4$. Remarkably, all these compositions show great improvements over the polyanion-free compositions (for example, $Li_{1.67}Mn_{1.5}Nb_{0.17}O_4$ and $Li_{1.93}Mn_{1.65}O_4$). Therefore, we conclude that the integrated rocksalt–polyanion structure presented in this Article is a general methodology to improve the stability of high-energy-density oxide cathodes, especially DRX cathodes.

Conclusions

We demonstrated a promising family of Co- and Ni-free DRXPS cathodes with stabilized high hybrid anion- and cation-redox capacities and energy densities. It overcomes the key bottleneck of poor high-voltage cyclability for the development of DRX cathodes and their derivatives. Despite the encouraging results, there remain issues to be addressed to enable the practical use of DRXPS cathodes. First, the ratio of the active materials in the composite cathode needs to be increased to >90 wt%, while the ratio of the conductive carbon needs to be substantially lowered for better practicality (for example, increase volumetric energy density, calculated in Supplementary Table 5). This can be resolved with a thin layer of uniform carbon coating, as is the case for LiFePO$_4$, which can improve the long-range electron percolation in the composite electrode. Second, the cycling stability needs to be further improved to allow for >500–1,000 deep charge–discharge cycles. This can be resolved by applying coatings, minor lattice doping, concentration-gradient design, and advanced electrolytes and electrolyte additives. With the above issues addressed, scalable synthesis methods (Supplementary Note 4) should be developed, and DRXPS cathodes should be evaluated in practical full cells (supported by pre-lithiation technologies for the first-cycle overlithiation). We look forward to rapid progress in developing Co- and Ni-free DRXPS cathodes, and their practical applications in sustainable energy.

Methods
Synthesis

All compositions were synthesized using a one-pot room-temperature mechanochemical synthesis method. Li_2O, Mn_2O_3, MnO_2, Li_3PO_4, Fe_2O_3, B_2O_3, Li_2SO_4 and SiO_2 (all from Sigma-Aldrich, 99% purity) precursors were directly mixed using the Fritsch Pulverisette 7 Premium Line planetary

ball mill, according to stoichiometry (for example, $Li_{1.67}Mn_{1.5}P_{0.17}O_4 = 0.58$ $Li_2O + 0.25 Mn_2O_3 + MnO_2 + 0.17 Li_3PO_4$). Precursor powders with a total weight of around 5 g were put into an 80 ml stainless-steel jar, with 25 10-mm-diameter stainless steel balls (the powder-to-ball weight ratio of was 1:20) and mixed in air at room temperature under 800 rpm for 5 h. No additional heat treatment was involved.

Materials characterizations

ICP-MS was conducted on Agilent 730. Inductively coupled plasma optical emission spectroscopy (ICP-OES) was conducted on Agilent 5100 VDV. High resolution X-ray diffraction data were collected at Beamline 11-BM, Argonne National Laboratory, in the 2θ range of 0.5–50° with a step size of 0.001°, counting time of 0.1 s per step, and a wavelength of $\lambda = 0.458961$ Å at 295 K and $\lambda = 0.458956$ Å at 100 K. Fine-ground polycrystalline powders were loaded into a φ0.8 mm Kapton capillary for installation on a magnetic sample base used by the beamline sample changer. The sample was spun continuously at 5,600 rpm during data collection. X-ray PDF measurements were completed at room temperature at the 11-ID beamline at the Advanced Photon Source, Argonne National Laboratory, using a General Electric amorphous Si two-dimensional detector. The sample to detect or distance was fixed at 117.13 mm, and synchrotron X-rays with the wavelength of 0.2127 Å were utilized with a 0.2 mm × 0.2 mm beam size. All other XRD measurements were conducted on an Aeris Research Edition X-ray diffractometer using a Cu target under 40 kV and 15 mA, in the 2θ range of 15–80°. Time-of-flight neutron diffraction was conducted at Multi Physics Instrument in China Spallation Neutron Source, operating at 160 kW beam power with 25 Hz repetition rate. About 3 g of powder was put into V can, and the measurement time was about 3 h. The diffraction dataset was analysed using GSAS II. Raman spectroscopy was conducted on WITec alpha300 R Raman microscope. Laser wavelength of 532 nm was applied with a power of 5 mW, a grating of 300 g mm⁻¹ and a spectral resolution of 0.1 cm⁻¹ to acquire the Raman data. Each spectrum was collected with five scans and 10 s integration for each scan. SEM was conducted on a Zeiss Merlin high-resolution scanning electron microscope. TEM, SAED and EDS were conducted on a JEOL 2010F transmission electron microscope with an acceleration voltage of 200 kV. Ex situ XANES measurement was conducted at the 7-BM beamline at the National Synchrotron Light Source II, Brookhaven National Laboratory, and at the BL17B1 beamline of the Shanghai Synchrotron Radiation Facility (SSRF), at a typical energy of the storage ring of 3.5 GeV under the 'top-up' mode with a constant current of 210 mA. HAADF-STEM and EELS mapping were performed using the TEAM I transmission electron microscope at the National Center for Electron Microscopy, Lawrence Berkeley National Laboratory. This microscope is double aberration-corrected and operates at 300 keV, with a convergence angle of 30 mrad and a beam current of 70 pA. A LASSO filter with thickness effect removal and a turbo colormap were applied to the HAADF-STEM image for better visualization of site occupations. The EELS mapping was acquired using a Gatan GIF Continuum K3 System. During the EELS measurement, the aperture size is 5 mm, yielding an EELS collection semi angle of 150 mrad, the dispersion is 0.18 eV Ch⁻¹ and the step size is 0.0996 nm. The grain selected for EELS measurement is close to a zone axis such that some lattice fringes can be seen. HAADF-STEM with EDS was performed using Thermo Fisher Scientific Themis Z G3 aberration-corrected scanning transmission electron microscope at MIT.Nano, operated at 200 kV with a beam current of 30–40 pA and 19 mrad convergence angle. EDS was collected with a 100 pA beam current on Super-X EDS detectors. X-ray fluorescence (XRF) was performed on a Bruker Tracer-III SD Portable XRF.

Electrochemical measurements

All electrodes for electrochemical testing were prepared by mixing 70 wt% active material, 20 wt% conductive carbon (Timcal Super C65) and 10 wt% polyvinylidene fluoride (Sigma-Aldrich) using N-methyl-2-pyrrolidone (Sigma-Aldrich) as the solvent to form a slurry, which was then casted onto an aluminium foil using a 250-μm-gap doctor blade. The loading of the electrode films was 2–3 mg cm⁻¹. A polypropylene (Celgard 2400) membrane was used as the separator, and 1.2 M LiPF₆ dissolved in ethylene carbonate:ethyl methyl carbonate = 30:70 wt% solution (Gotion) was used as the electrolyte. Li metal foil was used as the counter and reference electrode. Coin-type cells (CR2032) were assembled in an argon-filled glove box (MBraun). Electrochemical testing of the coin cells was conducted on a Landt CT2001A battery tester (Wuhan Lanhe Electronics) and a Neware battery tester (BTS-9000) at room temperature. Galvanostatic cycling was performed between 1.5 and 4.8 V versus Li/Li⁺ at 20 mA g⁻¹ for the initial two formation cycles, and then at 50 mA g⁻¹ onwards. The rate performance test was performed between 1.5 and 4.8 V versus Li/Li⁺ at 20, 50, 200, 500 and 1,000 mA g⁻¹ for five cycles each, on the same coin cell for each composition. GITT measurements were performed between 1.5 and 4.8 V versus Li/Li⁺, with 20 mA g⁻¹ current pulse for 20 min, followed by a 2 h relaxation step. For pouch cells, cathode film with active material loading of 2.5 mg cm⁻¹ and dimension of 3 cm × 4 cm was used, paired with Li metal foil. The electrolyte, separator and galvanostatic cycling test conditions were the same as coin cells. For XANES measurement, electrode samples were prepared by disassembling coin cells that were charged/discharged to a specific voltage, and then rinsed with dimethyl ether for 2 min. For ICP-OES measurement, electrolyte samples were prepared by disassembling coin cells after a certain number of cycles and charged to 4.8 V versus Li/Li⁺, and then soaking the cycled cathode film in fresh electrolyte for 10 days at room temperature. For ex situ and XRF measurements, cathode and anode films (lithium metal disc) were obtained by disassembling coin cells after a certain number of cycles and discharged to 3 V versus Li/Li⁺, and then rinsed with dimethyl ether for 2 min. In situ DEMS experiments were carried out using a commercial mass spectrometer (Linglu Instruments, Shanghai). The DEMS cell was assembled with a Swagelok-type cell, where the diameter and mass loading of the electrode disc were 16 mm and 10 mg cm⁻², respectively. The assembled cell was connected to the gas path of the mass spectrometer (Pfeiffer, OminiStar GSD 320). The total carrier gas (Ar) was 3 ml min⁻¹, and the flow was 3 ml min⁻¹ through the Swagelok cell. The cell was continuously ventilated for 6 h until the baseline was stable and then charged to 4.8 V versus Li/Li⁺ at a current density of 15 mA g⁻¹, and held at 4.8 V versus Li/Li⁺ for 4 h.

Data availability

The authors declare that all data supporting the findings of this study are available within the Article and its Supplementary Information files. Source data are provided with this paper.

References

1. Goodenough, J. B. & Kim, Y. Challenges for rechargeable Li batteries. *Chem. Mater.* **22**, 587–603 (2010).
2. Berg, E. J., Villevieille, C., Streich, D., Trabesinger, S. & Novak, P. Rechargeable batteries: grasping for the limits of chemistry. *J. Electrochem. Soc.* **162**, A2468–A2475 (2015).
3. Ahmed, S., Nelson, P. A., Gallagher, K. G., Susarla, N. & Dees, D. W. Cost and energy demand of producing nickel manganese cobalt cathode material for lithium-ion batteries. *J. Power Sources* **342**, 733–740 (2017).
4. Hirsh, H. S. et al. Sodium-ion batteries paving the way for grid energy storage. *Adv. Energy Mater.* **10**, 202001274 (2020).
5. Lee, J. et al. Unlocking the potential of cation-disordered oxides for rechargeable lithium batteries. *Science* **343**, 519–522 (2014).
6. Clement, R. J., Lun, Z. & Ceder, G. Cation-disordered rocksalt transition metal oxides and oxyfluorides for high energy lithium-ion cathodes. *Energ. Environ. Sci.* **13**, 345–373 (2020).
7. Ji, H. W. et al. Ultrahigh power and energy density in partially ordered lithium-ion cathode materials. *Nat. Energy* **5**, 213–221 (2020).

8. Lee, J. et al. Reversible Mn^{2+}/Mn^{4+} double redox in lithium-excess cathode materials. *Nature* **556**, 185 (2018).

9. Lun, Z. Y. et al. Cation-disordered rocksalt-type high-entropy cathodes for Li-ion batteries. *Nat. Mater.* **20**, 214 (2021).

10. Yabuuchi, N. et al. High-capacity electrode materials for rechargeable lithium batteries: Li_3NbO_4-based system with cation-disordered rocksalt structure. *Proc. Natl Acad. Sci. USA* **112**, 7650–7655 (2015).

11. Wang, R. et al. A disordered rocksalt Li-excess cathode material with high capacity and substantial oxygen redox activity: $Li_{1.25}Nb_{0.25}Mn_{0.5}O_2$. *Electrochem. Commun.* **60**, 70–73 (2015).

12. Xue, W. J. et al. Ultra-high-voltage Ni-rich layered cathodes in practical Li metal batteries enabled by a sulfonamide-based electrolyte. *Nat. Energy* **6**, 495–505 (2021).

13. Zhu, Z. et al. Gradient-morph $LiCoO_2$ single crystals with stabilized energy density above 3400 W h L^{-1}. *Energ. Environ. Sci.* **13**, 1865–1878 (2020).

14. Armstrong, A. R. et al. Demonstrating oxygen loss and associated structural reorganization in the lithium battery cathode $Li[Ni_{0.2}Li_{0.2}Mn_{0.6}]O_2$. *J. Am. Chem. Soc.* **128**, 8694–8698 (2006).

15. Yoon, M. et al. Unveiling nickel chemistry in stabilizing high-voltage cobalt-rich cathodes for lithium-ion batteries. *Adv. Funct. Mater.* **30**, 201907903 (2020).

16. Zhu, Z. et al. Gradient Li-rich oxide cathode particles immunized against oxygen release by a molten salt treatment. *Nat. Energy* **4**, 1049–1058 (2019).

17. Dong, Y., Liang, Q., Alvarez, A., Li, J. & Chen, I.-W. Enhanced mobility of cations and anions in the redox state: the polaronium mechanism. *Acta Mater.* **232**, 117941 (2022).

18. Yan, P. F. et al. Injection of oxygen vacancies in the bulk lattice of layered cathodes. *Nat. Nanotechnol.* **14**, 602 (2019).

19. Lee, J. et al. Determining the criticality of Li-excess for disordered-rocksalt Li-ion battery cathodes. *Adv. Energy Mater.* **11**, 2100204 (2021).

20. Hao Li, R. F. et al. Toward high-energy Mn-based disordered-rocksalt Li-ion cathodes. *Joule* **6**, 53–91 (2022).

21. Lee, E. S. & Manthiram, A. Smart design of lithium-rich layered oxide cathode compositions with suppressed voltage decay. *J. Mater. Chem. A* **2**, 3932–3939 (2014).

22. Christian, M., Julien, A. M., Zaghib, K. & Groult, H. Comparative issues of cathode materials for Li-ion batteries. *Inorganics* **2**, 132–154 (2014).

23. Radin, M. D. et al. Narrowing the gap between theoretical and practical capacities in Li-ion layered oxide cathode materials. *Adv. Energy Mater.* **7**, 201602888 (2017).

24. Zhang, W. J. Structure and performance of $LiFePO_4$ cathode materials: a review. *J. Power Sources* **196**, 2962–2970 (2011).

25. Manthiram, A. & Goodenough, J. B. Lithium-based polyanion oxide cathodes. *Nat. Energy* **6**, 844–845 (2021).

26. Manthiram, A. A reflection on lithium-ion battery cathode chemistry. *Nat. Commun.* **11**, 1–9 (2020).

27. Sawamura, M. et al. Nanostructured $LiMnO_2$ with Li_3PO_4 integrated at the atomic scale for high-energy electrode materials with reversible anionic redox. *ACS Cent. Sci.* **6**, 2326–2338 (2020).

28. House, R. A. et al. Superstructure control of first-cycle voltage hysteresis in oxygen-redox cathodes. *Nature* **577**, 502–508 (2020).

29. Sumita, M., Tanaka, Y., Ikeda, M. & Ohno, T. Theoretically designed Li_3PO_4 (100)/$LiFePO_4$ (010) coherent electrolyte/cathode interface for all solid-state Li-ion secondary batteries. *J. Phys. Chem. C* **119**, 14–22 (2015).

30. Gnewuch, S. & Rodriguez, E. E. Distinguishing the intrinsic antiferromagnetism in polycrystalline $LiCoPO_4$ and $LiMnPO_4$ olivines. *Inorg. Chem.* **59**, 5883–5895 (2020).

31. Chung, H. T., Myung, S. T., Cho, T. H. & Son, J. T. Lattice parameter as a measure of electrochemical properties of $LiMn_2O_4$. *J. Power Sources* **97**, 454–457 (2001).

32. Li, T., Chang, K., Hashem, A. M. & Julien, C. M. Structural and electrochemical properties of the high Ni-content spinel $LiNiMnO_4$. *Electrochem* **2**, 95–117 (2021).

33. Akimoto, J. & Gotoh, Y. Single crystal growth, structure and physical property of $LiCoO_2$ and $LiNiO_2$. *Mol. Cryst. Liq. Cryst.* **341**, 947–950 (2000).

34. de Biasi, L. et al. Chemical, structural, and electronic aspects of formation and degradation behavior on different length scales of Ni-rich NCM and Li-rich HE-NCM cathode materials in Li-ion batteries. *Adv. Mater.* **31**, 201900985 (2019).

35. Markevich, E. et al. Raman spectroscopy of carbon-coated $LiCoPO_4$ and $LiFePO_4$ olivines. *J. Power Sources* **196**, 6433–6439 (2011).

36. Julien, C. M. & Massot, M. Lattice vibrations of materials for lithium rechargeable batteries. III. Lithium manganese oxides. *Mater. Sci. Eng. B* **100**, 69–78 (2003).

37. Wu, J. et al. In situ Raman spectroscopy of $LiFePO_4$: size and morphology dependence during charge and self-discharge. *Nanotechnology* **24**, 424009 (2013).

38. Tang, D. et al. Electrochemical behavior and surface structural change of $LiMn_2O_4$ charged to 5.1 V. *J. Mater. Chem. A* **2**, 14519–14527 (2014).

39. Tang, D. et al. Surface structure evolution of $LiMn_2O_4$ cathode material upon charge/discharge. *Chem. Mater.* **26**, 3535–3543 (2014).

40. Manceau, A., Marcus, M. A. & Grangeon, S. Determination of Mn valence states in mixed-valent manganates by XANES spectroscopy. *Am. Mineral.* **97**, 816–827 (2012).

Acknowledgements

Author contributions

Y. Huang, Y.D. and J. Li conceived the project. Y. Huang synthesized the materials and conducted XRD, SEM, ICP-OES and XRF measurements. Y. Huang, M.Y., S.L., E.Y.Z., Y.L. and H.J. contributed to electrochemical testing. Y.Y., Y.S., Y. Han, J.C., C.O., C.S. and A.P. contributed to sample preparations, data collection and data processing for HAADF-STEM and EELS. T.L. contributed to high-resolution XRD and PDF measurements. W.H.K., H.C. and W.Y. contributed to neutron powder diffraction measurements. Y.P. and M.L. contributed to DEMS measurements. B.W. contributed to TEM imaging, SAED and STEM–EDS. B.W., Z.C., Y.Z. and H.J. contributed to Raman measurements. Z.C. and J.X contributed to ICP-MS measurements. L.M., X.X. and L.G. contributed to XANES measurements. W.L., R.M. and C.Y. contributed to XRD Rietveld

refinement. Y. Huang and Y.D. analysed the data. Y. Huang, Y.D. and J. Li wrote the paper. All authors discussed and contributed to the writing.

Competing interests

Y. Huang, Y.D. and J. Li report a US non-provisional patent application filed by the Massachusetts Institute of Technology, patent application no. 18/790,946. The patent is related to the compositions and synthesis method reported in this Article. The other authors declare no competing interests.

Additional information

Supplementary information The online version contains supplementary material available at https://doi.org/10.1038/s41560-024-01615-6.

Correspondence and requests for materials should be addressed to Yanhao Dong or Ju Li.

Peer review information *Nature Energy* thanks Wei Kong Pang and the other, anonymous, reviewer(s) for their contribution to the peer review of this work.

Reprints and permissions information is available at www.nature.com/reprints.

Publisher's note Springer Nature remains neutral with regard to jurisdictional claims in published maps and institutional affiliations.

Springer Nature or its licensor (e.g. a society or other partner) holds exclusive rights to this article under a publishing agreement with the author(s) or other rightsholder(s); author self-archiving of the accepted manuscript version of this article is solely governed by the terms of such publishing agreement and applicable law.

© The Author(s), under exclusive licence to Springer Nature Limited 2024

[1]Department of Materials Science and Engineering, Massachusetts Institute of Technology, Cambridge, MA, USA. [2]State Key Laboratory of New Ceramics and Fine Processing, School of Materials Science and Engineering, Tsinghua University, Beijing, China. [3]Department of Nuclear Science and Engineering, Massachusetts Institute of Technology, Cambridge, MA, USA. [4]Department of Engineering Science and Mechanics and Materials Research Institute, The Pennsylvania State University, University Park, PA, USA. [5]Chemical Sciences and Engineering Division, Argonne National Laboratory, Argonne, IL, USA. [6]Department of Chemical and Biological Engineering, Gachon University, Seongnam-si, Republic of Korea. [7]Department of Mining and Materials Engineering, McGill University, Montréal, Quebec, Canada. [8]National Center for Electron Microscopy, Molecular Foundry, Lawrence Berkeley National Laboratory, Berkeley, CA, USA. [9]MIT.Nano, Massachusetts Institute of Technology, Cambridge, MA, USA. [10]Department of Materials Science and Engineering, Huazhong University of Science and Technology, Wuhan, China. [11]Department of Chemistry, Department of Materials Science, Shanghai Key Laboratory of Molecular Catalysis and Innovative Materials, Fudan University, Shanghai, China. [12]National Synchrotron Light Source II, Brookhaven National Laboratory, Upton, NY, USA. [13]Spallation Neutron Source Science Center, Dongguan, China. [14]Institute of High Energy Physics, Chinese Academy of Sciences, Beijing, China. [15]Shanghai Synchrotron Radiation Facility, Shanghai Advanced Research Institute, Chinese Academy of Sciences, Shanghai, China. [16]Department of Chemical Engineering, R&D Center for Membrane Technology, Center for Circular Economy, Chung Yuan Christian University, Taoyuan City, Taiwan ROC. [17]Department of Physics, National Central University, Taoyuan City, Taiwan ROC. ✉e-mail: dongyanhao@tsinghua.edu.cn; liju@mit.edu